



Coherent spin waves driven by optical spin-orbit torque

Gyung-Min Choi ^{1,2,*}, Dong-Kyu Lee,³ Kyung-Jin Lee,^{3,4} and Hyun-Woo Lee ⁵

¹*Department of Energy Science, Sungkyunkwan University, Suwon 16419, Korea*

²*Center for Integrated Nanostructure Physics, Institute for Basic Science (IBS), Suwon 16419, Korea*

³*Department of Materials Science and Engineering, Korea University, Seoul 02841, Korea*

⁴*KU-KIST Graduate School of Converging Science and Technology, Korea University, Seoul 02841, Korea*

⁵*Department of Physics, Pohang University of Science and Technology, Pohang 37673, Korea*



(Received 24 March 2020; revised 18 May 2020; accepted 18 June 2020; published 21 July 2020)

Phase-coherent spin waves can be generated by magnetic field pulse, spin current pulse, or optical pulse. Here we use optical spin-orbit torque, originating from the conversion of an optical pulse into a spin-polarized current pulse, to excite spin waves in the frequency range from GHz to THz. We investigate the frequency, amplitude, and damping of the spin waves of Co thin films. From the frequency analysis, we determine the stiffness of Co spin waves to be 5 meV nm^2 . From the amplitude analysis, we show that the Co layer acts as a cavity for spin waves. From the damping analysis, we observe that the damping enhancement due to the spin pumping effect is about two times larger in spin waves than in uniform precession.

DOI: [10.1103/PhysRevB.102.014437](https://doi.org/10.1103/PhysRevB.102.014437)

I. INTRODUCTION

Spin waves are a fundamental excitation that explain the thermodynamic properties of ferromagnetic (or antiferromagnetic) phases [1–3]. In application, spin waves can have a passive role in spintronic devices for phase locking of spin-torque oscillators [4,5]. Recently, spin wave has been considered as an active element for computing devices such as an information carrier or signal processing element [6–13]. Such progress in the fundamental study and practical application of spin waves has led to the emerging research area of magnonics [14–16].

For use as an information carrier, a phase-coherent spin wave is required. In addition, for device scalability to the nanometer scale, spin waves with THz frequency are desirable. Previously, phase-coherent spin waves have been generated by oscillating magnetic fields or electrical spin injection [17,18]. However, these conventional methods have a frequency limit of a few tens of GHz because the timescale of the magnetic field or electric current pulse is on the order of micro- to nanoseconds. Alternatively, an optical pulse may be employed, but the frequency of the excited spin waves has so far been limited to a few tens of GHz [19–21]. Recently, THz spin waves have been excited by converting an optical pulse into a spin-polarized current pulse in FM/NM/FM trilayers, where FM is a ferromagnetic metal, and NM is a normal metal [22–24]. When an optical pulse creates a spin-polarized current pulse via ultrafast demagnetization of the first FM, the second FM, whose magnetization is noncollinear with that of the first FM, absorbs the spin-polarized current [25,26]. Since the spin-polarized current pulse can be shorter than 1 ps, THz spin waves can be excited. However, the analysis of spin waves demands detailed characterizations of both FMs

and their coupling because not only the first FM but also the second may affect the spin wave signals.

In this work, we employ an optical spin-orbit torque (OSOT) to excite coherent spin waves up to THz frequency in a Co/Pt bilayer, where only one FM is present (Fig. 1). The optical orientation on Pt converts an optical pulse into a spin-polarized current pulse [27]. The spin-polarized current is absorbed by Co and excites not only uniform precession but also spin waves with finite wave numbers. Since only one FM is present, the analysis of spin wave in the FM/HM, (where HM is a heavy metal), bilayer is relatively straightforward compared to an FM/NM/FM structure. For instance, the FM/HM system provides a good platform to examine the damping of spin waves. In this work, we show the damping of spin waves in the FM/HM structure has a linear relationship with $1/d$, where d is the FM thickness, while a more complicated behavior was observed with the FM/NM/FM structure [24]. We investigate the frequency, amplitude, and damping of spin waves in the frequency range from GHz to THz. From the frequency analysis, we determine the spin wave stiffness and compare it with previous reports. From the amplitude analysis, we show that the amplitude ratio between spin waves and uniform precession is larger than two, which indicates that FM acts as a cavity for spin waves. From the damping analysis, we observe a clear dependence on the FM thickness, which is attributed to the spin pumping effect of spin waves.

II. EXPERIMENT

We study samples of the film structures of sap/Co ($3 \sim 30 \text{ nm}$)/Pt (2 nm) and sap/Pt (2 nm)/Co (10 nm), where the sap is a sapphire substrate with (0001) texture. All layers are deposited by magnetron sputtering with a base pressure of $< 1 \times 10^{-7}$ Torr without breaking the vacuum. The Co layers of all samples have an in-plane magnetic anisotropy. To generate and detect the OSOT, we use a time-resolved

*Corresponding author: gmchoi@skku.edu

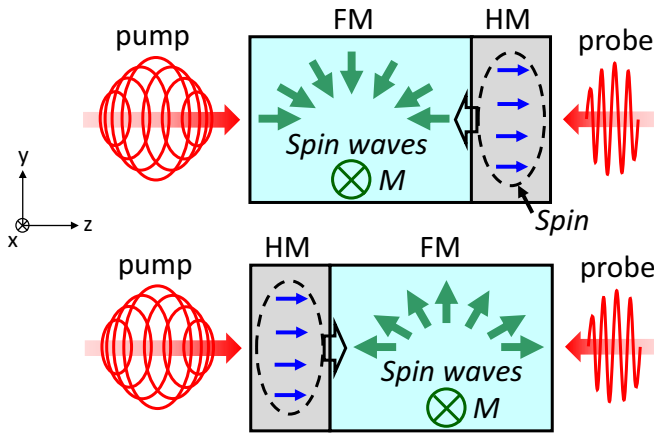


FIG. 1. Schematics of the experiment. A circularly polarized pump generates spin-polarized electrons (blue arrows), whose spin angular momentum in HM is along the z direction. A spin transport from HM to FM excites spin waves (green arrows) in FM, whose initial magnetization (M) lies to the x direction. A linearly polarized probe detects the z component of the spin waves. The top and bottom panels correspond to the sap/FM/HM and sap/HM/FM structure, respectively.

pump-probe technique. To generate the OSOT, a circularly polarized pump light with a photon energy of 1.58 eV and a pulse width of 1.1 ps is incident on the substrate side of the samples (Co side for the sap/Co/Pt structure and Pt side for the sap/Pt/Co structure): the pump passes the substrate and Co layer, then is absorbed by the Pt layer; the Pt layer converts the pump pulse to a spin-polarized current pulse; the spin-polarized current pulse is injected into the Co layer and induces magnetization dynamics (Fig. 1). The initial magnetization of Co is aligned to the x direction by an external magnetic field of 0.06 T. To detect the magnetization dynamics of Co, a linearly polarized probe light with pulse width of 0.2 ps is incident on the surface side (Pt side for the sap/Co/Pt structure and Co side for the sap/Pt/Co structure) of the samples and measures the z component of magnetization by the polar mag-

netooptical Kerr effect (MOKE). When we use both sap/Co/Pt and sap/Pt/Co structures, the spin wave signal is higher with sap/Co/Pt than with sap/Pt/Co at a Pt thickness of 2 nm. The raw data contain both pump-helicity-dependent and pump-helicity-independent signals. The helicity-dependent signal is collected by taking the difference between right-circular polarization and left-circular polarization of the pump. All experiments are performed at room temperature with an incident pump fluence of 10 J m^{-2} . We confirm the measured signal is linearly proportional to the pump fluence (Appendix A).

III. RESULTS AND DISCUSSION

A. OSOT-driven magnetization dynamics

We excite the magnetization dynamics in Co using OSOT: optical spin generation on Pt and subsequent spin transport from Pt to Co. The excited magnetization dynamics have two components: slow and fast dynamics [Fig. 2(a)]. In our previous study, we showed that the slow dynamic comes from the uniform precession of magnetization of Co [27]. The uniform precession can be fitted with a damped cosine function of $\pm A \cos(2\pi f t) \exp(-t/\tau)$, where A is the amplitude, f is the frequency, t is the time, and τ is the relaxation time. The \pm sign of the uniform precession is determined by the helicity of pump light, but it does not depend on the direction from which the probe light is incident (either Pt side for the sap/Co/Pt structure or Co side for the sap/Pt/Co structure). On the other hand, the fast dynamics changes its sign when measured from opposite sides of the heterostructure [Fig. 2(b)]. (Only the probe position determines the sign of the fast dynamics, and it is unaffected by the pump.) This result suggests that the fast dynamic derives from the spatial variation of magnetization dynamics.

B. Frequency of spin waves

We measure the frequency of the magnetization dynamics by varying the Co thickness. (Extracting the fast dynamics from the raw data is shown in Appendix B.) While the slow dynamics frequency does not show much dependence on Co

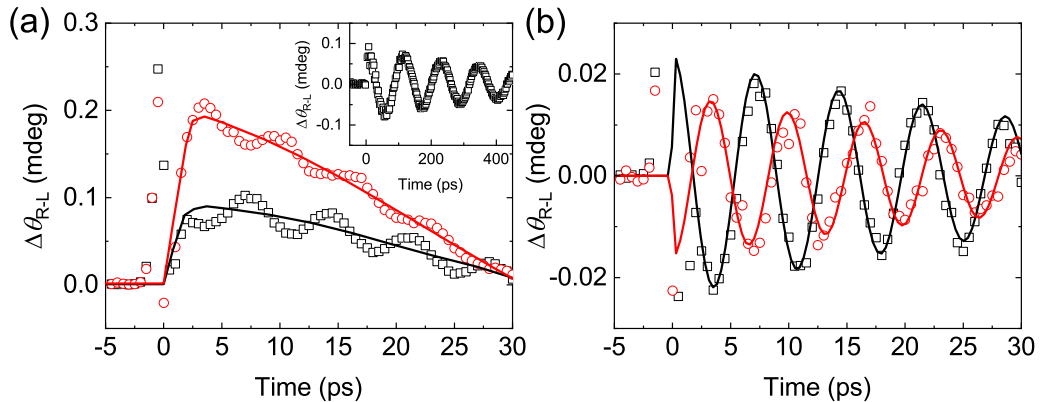


FIG. 2. Slow and fast dynamics of magnetization. (a) The OSOT-driven dynamics of the Co magnetization of the sap/Co (10 nm)/Pt (2 nm) (black squares) and sap/Pt (2 nm)/Co (10 nm)/MgO (3 nm) (red circles) samples. A fast oscillation exists on top of a slow oscillation. Black and red lines are guides for the slow oscillation. The inset shows the slow oscillation of the sap/Co (10 nm)/Pt (2 nm) sample up to 450 ps. (b) The subtracted fast oscillation of the sap/Co (10 nm)/Pt (2 nm) (black squares) and sap/Pt (2 nm)/Co (10 nm)/MgO (3 nm) (red circles) samples. The solid lines are fittings with damped cosine function with a frequency of 140 GHz (black line) and 150 GHz (red line).

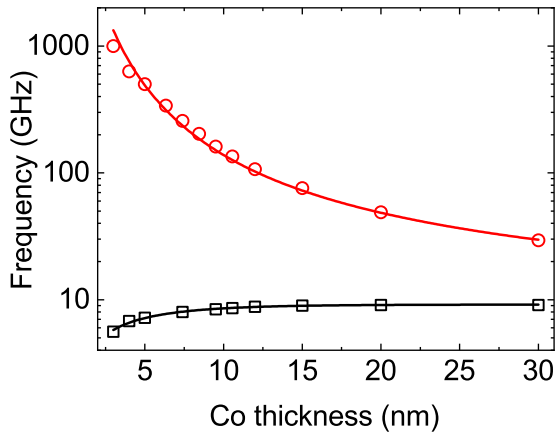


FIG. 3. Frequency analysis. Frequency of the FMR mode (black squares) and spin waves (red circles) of the sap/Co (x nm)/Pt(2 nm) samples. The black line is a result of Eq. (1) with $k = 0$ and $\mu_0 M_{\text{eff}}$ (unit of Tesla) of $1.41 - 1.73 \times \exp(-x/4.51)$, where x is the Co thickness in the unit of nm. The red line is a result of Eq. (1) with $k = \pi/d_{\text{Co}}$ and D of 5 meV nm^2 .

thickness (d_{Co}), the fast dynamics frequency increases rapidly with decreasing d_{Co} : increasing from 29 GHz at 30 nm Co to 1 THz at 3 nm Co (Fig. 3). The frequency (f) of both slow and fast dynamics can be explained by [22]:

$$f = \frac{\gamma}{2\pi} \sqrt{\left(\frac{Dk^2}{\gamma\hbar} + \mu_0 H_{\text{ext}} \right) \left(\frac{Dk^2}{\gamma\hbar} + \mu_0 (H_{\text{ext}} + M_{\text{eff}}) \right)}, \quad (1)$$

where γ is the gyromagnetic ratio, which is $1.94 \times 10^{11} \text{ rads}^{-1} \text{ T}^{-1}$ with the g factor of 2.2 [28], D is the spin wave stiffness, k is the wavevector of spin waves, \hbar is the reduced Planck constant, $\mu_0 H_{\text{ext}}$ is the external magnetic field of 0.06 T, and $\mu_0 M_{\text{eff}}$ is the effective dipolar field, which is determined by magnetic anisotropy (including shape, crystalline, and surface anisotropy). (We determine the $\mu_0 M_{\text{eff}}$ value from the frequency of the slow dynamics of Fig. 3 to use it for the damping analysis later.) The slow dynamics corresponds to the ferromagnetic resonance (FMR) mode with $k = 0$. The fast dynamics corresponds to the standing spin wave oscillation in FM with half a wavelength along the FM thickness direction with $k = \pi/d_{\text{Co}}$. From the spin wave frequency, we determine a D of 5 meV nm^2 , which is consistent with the previous report for hcp Co using neutron scattering [29,30] and Brillouin light scattering [31–33]. However, we note that our result of $D = 5 \text{ meV nm}^2$ is considerably smaller than a recent reported value of 8.8 meV nm^2 obtained with a FM/NM/FM structure [24].

C. Amplitude of spin waves

Next, we investigate the amplitude of the spin wave. For this, we compare the measured amplitudes of the FMR mode ($k = 0$) and the spin wave mode ($k = \pi/d$). With the sap/Co (10 nm)/Pt (2 nm) structure, the measured amplitude ratio between spin wave and FMR is ≈ 0.3 (Appendix A). The actual amplitude of the spin waves should be much larger than the measured value considering the surface sensitivity

of our optical system. Because the wavelength of spin wave is comparable or even smaller than the penetration depth of probe light, the surface sensitivity for spin wave is less than one. Calculating the surface sensitivity with refractive indexes and magneto-optical constants of each layer [Fig. 4(a)], we determine the actual ratio between the spin wave and FMR mode [Fig. 4(b)]. (A detailed explanation for the calculation of the surface sensitivity is shown in Appendix C.) The actual ratio is higher than two at Co thickness greater than 10 nm. This result shows that a thin ferromagnet acts as a cavity that amplifies spin waves with specific wave vectors. At Co thickness smaller than 10 nm, the magnitude of spin wave diminishes quickly because of the reduced phase coherence. When the pulse width of light becomes comparable with the period of the spin wave, the phase coherence of the excited spin wave decreases [Fig. 4(a)]. (A detailed explanation for the calculation of the phase coherence is shown in Appendix D.)

We also check the magnitude of spin wave using a micromagnetic simulation with the parameters determined from experiments. When a spin current pulse (pulse width 1 ps) is injected into Co, both FMR mode and spin wave modes are excited [Fig. 4(c)]. We compare the amplitudes of $k = 0$ and $k = \pi/d_{\text{Co}}$ modes by integrating peaks of Fourier transforms of the micromagnetic results. For $d_{\text{Co}} > 10 \text{ nm}$, surprisingly, the amplitude of $k = \pi/d_{\text{Co}}$ mode is ≈ 2.3 times larger than that of $k = 0$ mode. It is known that a spin current, whose polarization is transverse to the magnetization direction, is absorbed by magnetization near the interface [34]. The spin attenuation along the FM thickness is described with a spin dephasing length (λ), which is often less than 1 nm [34]. We find that the amplitude ratio depends on λ . At a Co thickness of 10 nm, the amplitude ratio varies from 2.5 with λ of 0 (full spin absorption by the first monolayer of Co) to 2.3 with λ of 1 nm. For Co thickness less than 10 nm, the amplitude ratio decreases because the phase coherency of magnons deteriorates. This enhanced amplitude for a finite k mode is well described by the spin wave stiffness (Appendix E). Therefore, even at a fixed thickness of FM, we can determine the spin wave stiffness from the amplitude analysis of spin wave.

D. Damping of spin waves

Lastly, we examine the damping of spin waves. We fit the FMR and spin wave data with a damped cosine function of $\cos(2\pi ft) \times \exp(-t/\tau)$, where t is time, and τ is the relaxation time [Fig. 5(a)]. From the fitting results of the relaxation time, we determine the damping parameters of FMR (α_{FMR}) and spin wave (α_{sw}) by [24]:

$$\alpha^{-1} = \gamma\tau \left(\mu_0 H_{\text{ext}} + \frac{\mu_0 M_{\text{eff}}}{2} + \frac{Dk^2}{\gamma\hbar} \right). \quad (2)$$

α_{FMR} is obtained using τ of the FMR oscillation and Eq. (2) with $k = 0$. α_{sw} is obtained using τ of the spin wave oscillation and Eq. (2) with $k = \pi/d_{\text{Co}}$. Both α_{FMR} and α_{sw} increase with decreasing Co thickness [Fig. 5(b)]. We note that our result is quite different from a recent result for a [Co/Ni]/Cu/Co(d) trilayer, where the damping of spin wave shows a peak value of 0.3 at Co of 10 nm and then decreases at smaller thickness [24]. We expect that the damping behavior

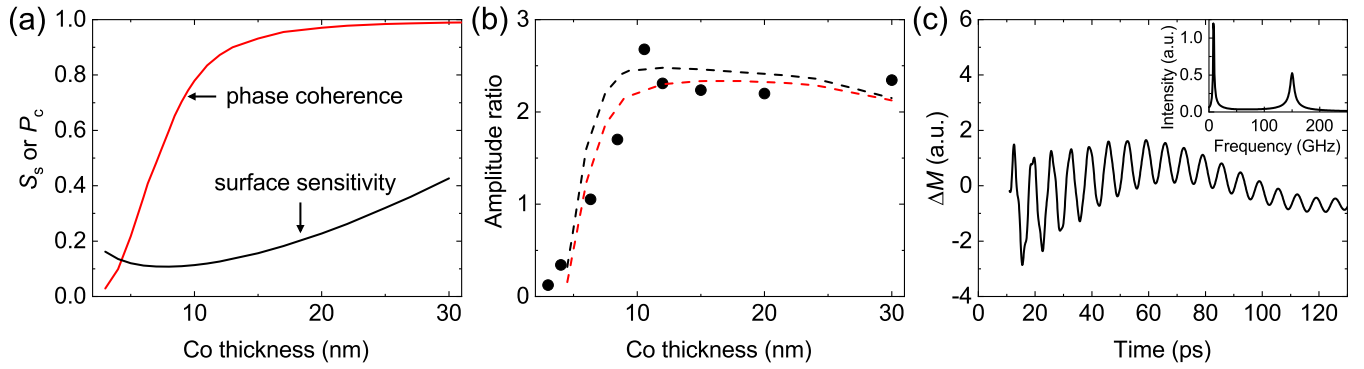


FIG. 4. Amplitude analysis. (a) Surface sensitivity (S_s) due to a finite penetration depth of probe (black line). Phase coherence (P_c) due to a finite pulse width of the pump (red line). (b) Actual amplitude ratio between the spin waves ($k_1 = \pi/d$) and FMR mode ($k_0 = 0$) determined experimentally (black circles) and from the micromagnetic simulation (black and red dotted lines) of the sap/Co (x nm)/Pt(2 nm) structure. The black and red color indicate the spin dephasing length of 0 and 1 nm, respectively. (c) Micromagnetic simulation for the surface magnetization of Co in the sap/Co (10 nm)/Pt (2 nm). The inset is the Fourier transform result of (c). The peaks at 9 GHz and 150 GHz correspond to the FMR mode and spin wave, respectively.

in the FM/NM/FM structure would be more complicated because of the interaction between two ferromagnets.

The thickness dependence of the FMR mode damping is well understood with a spin pumping theory: a uniform precession of magnetization of Co generates a spin current to Pt [35,36].

$$\alpha = \alpha_0 + \frac{A_{\text{sp}}}{d_{\text{Co}}}, \quad (3)$$

where α_0 is the intrinsic damping, and A_{sp} is the interfacial spin pumping. From the linear fitting of α_{FMR} at the Co thickness range of 5 ~ 15 nm, we determine α_0 of 0.006 and A_{sp} of 0.11 nm^{-1} for the FMR mode, which are consistent with previous reports [24,35]. We also apply Eq. (3) to the damping of spin waves. From the linear fitting of α_{sw} , we determine α_0 of 0.003 and A_{sp} of 0.19 nm^{-1} for the spin wave mode. (We exclude data at Co thickness less than 4 nm, where an abnormal increase in damping is observed.) From the fitting result of A_{sp} , we interpret that the spin pumping effect is about two times larger in spin waves than in FMR mode. There have been several theoretical efforts to extend the spin pumping

theory to the spin waves [37,38]. Specifically, Kapelrud *et al.* theoretically investigated the spin pumping in a ferromagnetic insulator/normal metal structure and showed that spin waves, which are standing waves along with the thickness with a small in-plane wave vector, have damping enhancement that is twice that of the FMR mode [37]. Although it was developed for ferromagnetic insulators, we expect this theory can be extended to ferromagnetic metals as well. However, when Co thickness is too thick or too thin, the measurements deviate from the linear relationship of Eq. (3). At Co thickness of ≥ 15 nm, a saturation of damping is observed, and at Co thickness of ≤ 4 nm, a further enhancement of damping is observed. Other mechanisms, such as interface scattering and coupling with Stoner excitation [39], may participate at a range of small thickness. In addition, spin diffusion length of Co, which was reported to be 5 ~ 8 nm at room temperature [40,41], might affect the efficiency of the spin pumping. For a detailed analysis in this range, reliable data points up to Co thickness of 1 nm are required, which, however, goes beyond the scope of this paper.

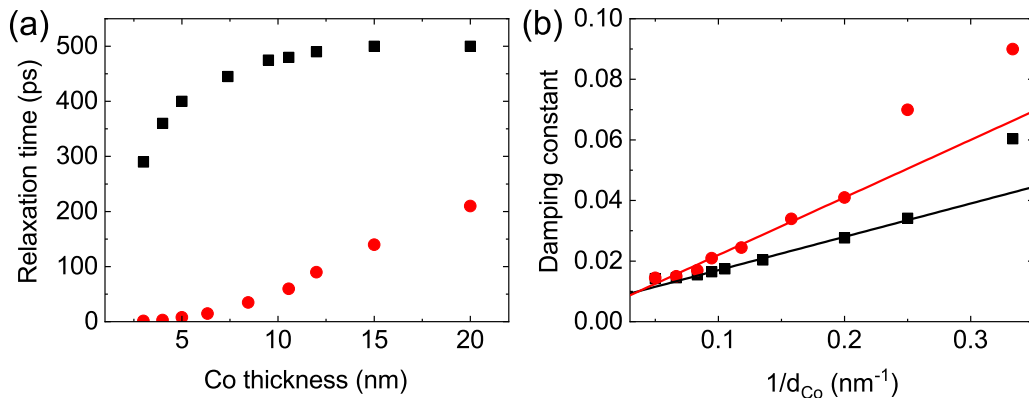


FIG. 5. Damping analysis. (a) Relaxation time (τ) of FMR mode (black squares) and spin wave (red circles) of fittings with damped cosine function of the sap/Co (x nm)/Pt(2 nm) samples. (b) Damping constant (α) of FMR mode (black squares) and spin wave (red circles) determined from τ of (a) and Eq. (2). The black (red) line is fitting of the Eq. (3) with α_0 of 0.006 (0.003) and A_{sp} of 0.11 (0.19).

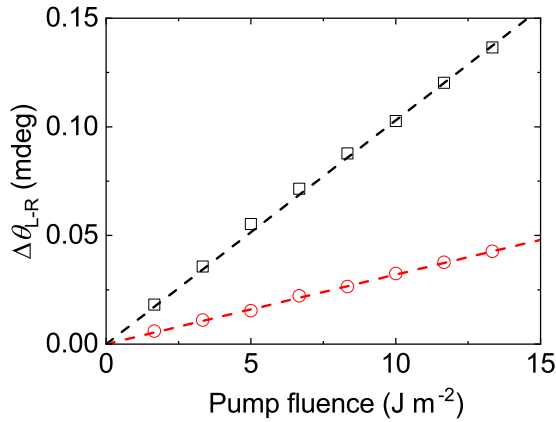


FIG. 6. Pump fluence dependence on amplitudes of FMR mode (black squares) and spin wave (red circles) of the sap/Co (10 nm)/Pt (2 nm) sample. Dashed lines are linear fits to data.

IV. CONCLUSION

We demonstrate that optical spin-orbit torque in an FM/HM structure is a useful tool to excite the high-frequency coherent spin waves in FM. The frequency analysis gives information about the spin wave stiffness. The amplitude analysis demonstrates that ferromagnets act as cavities and amplify the resonant mode of spin waves. The amplitude ratio between FMR mode and spin wave is determined by the spin wave stiffness. The damping analysis shows an increasing trend with decreasing Co thickness. Importantly, the damping of spin waves increases two times faster than that of FMR mode. We interpret the damping enhancement as a result of the spin pumping effect of spin waves.

ACKNOWLEDGMENTS

G.-M.C. acknowledges the National Research Foundation of Korea (NRF) grant funded by the Korea government (MSIP) (NRF-2019R1C1C1009199) and the Creative Materials Discovery Program through the National Research Foundation of Korea (NRF) funded by Ministry of Science

and ICT (2018M3D1A1058793). K.-J.L. acknowledges the NRF (NRF-2020R1A2C3013302). H.-W.L. acknowledges the NRF (NRF-2020R1A2C2013484).

APPENDIX A: PUMP FLUENCE DEPENDENCE

We check pump fluence dependence on amplitude of FMR mode ($k = 0$) and spin wave ($k = \pi/d$) of the sap/Co (10 nm)/Pt (2 nm) sample. Both uniform precession and magnon dynamics show a linear dependence on pump fluence (Fig. 6). At the same pump fluence, the measured amplitude of the spin wave is about three times smaller than that of FMR mode.

APPENDIX B: EXTRACTING SPIN WAVE SIGNALS

We obtain the spin wave signal by subtracting the uniform precession signal from the raw data. The uniform precession signal is adjusted to be smooth in time and does not leave any offset in the spin wave signal. Representative procedures for extracting the spin wave signal are shown in Fig. 7.

APPENDIX C: SURFACE SENSITIVITY

Polarization of probe light can interact with the phase of spin waves because the probe sees magnetization nonuniformly along with the thickness. We calculate the surface sensitivity of the probe using the transfer matrix method with refractive indexes and magneto-optical constants of sap/Co (10 nm)/Pt (2 nm) structure. The magneto-optical constant of Co is $-0.03 + i0.02$ [42]. Although Pt is nonmagnetic, it becomes magnetic at the Co interface with a length scale of ~ 0.5 nm due to proximity effect [43]. The induced magnetism of Pt can increase or decrease the surface sensitivity of probe depending on the location of Pt. For simplicity, we divide Pt of 2 nm thickness into two regions: a 0.5 nm-thick magnetic region in contact with Co and a 1.5 nm-thick nonmagnetic region. We determine the magneto-optical constant of the magnetic 0.5 nm-thick region to be 1.8 times the magneto-optical constant of Co considering that the amplitude ratio between magnon signal and uniform precession is ~ 5 times smaller

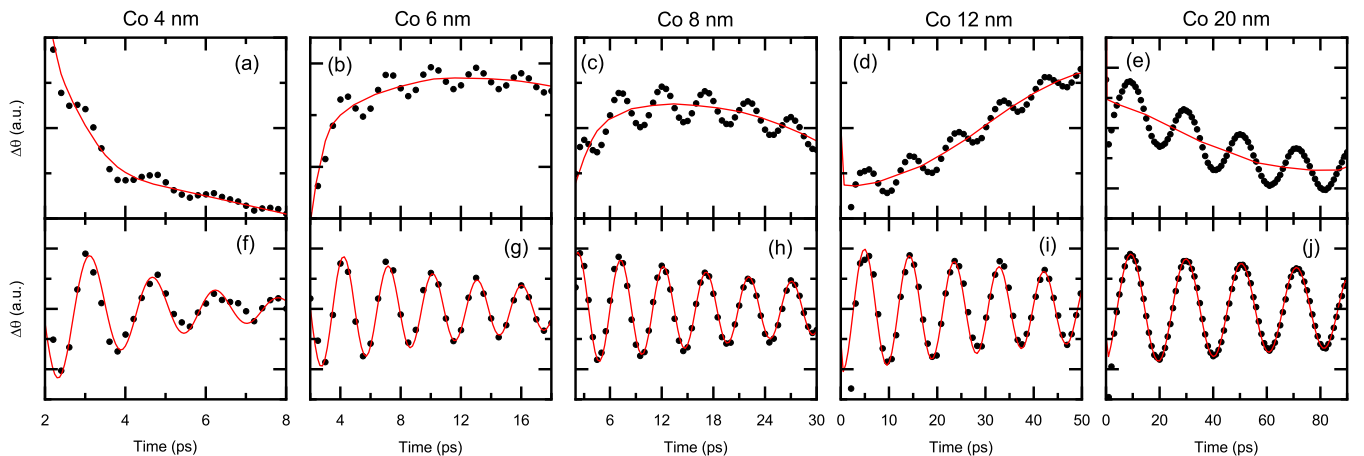


FIG. 7. Extracting the spin wave signal from the raw data. Top panels show the raw data of the Kerr rotation with Co thickness of (a) 4, (b) 6, (c) 8, (d) 12, and (e) 20 nm. Red lines are guides for the slow dynamics. Bottom panels show the extracted spin wave signal with Co thickness of (f) 4, (g) 6, (h) 8, (i) 12, and (j) 20 nm. Red lines are fittings with a damped cosine function.

with the sap/Pt (2 nm)/Co (10 nm)/MgO (3 nm) than with the sap/Co (10 nm)/Pt (2 nm). The calculated result of the surface sensitivity of the sap/Co (x nm)/Pt(2nm) structure is shown as Fig. 4(a) in the main text.

APPENDIX D: PHASE COHERENCY

A finite pulse width of the pump and probe reduces phase coherency of the magnon when the pulse width becomes comparable with the period of the spin wave oscillation [44]. Since pulse width of the pump is much wider than that of the probe, the phase coherency is mostly limited by the pump. The phase coherency of magnon can be determined by,

$$\int_{-\infty}^{\infty} I_p(t) \cos(\omega t) dt, \quad (\text{D1})$$

where $I_p(t)$ is the normalized pump power with a pulse width of 1.1 ps, t is the time, $\omega \approx Dk^2/\hbar$ is the angular frequency of magnon, D is the spin wave stiffness of Co, $k = \pi/d$ is the wave vector of magnon, and d is the thickness of Co. When Co is thicker than 10 nm, the phase coherency is close to one. However, when Co becomes thinner than 10 nm, the phase coherency quickly decreases. For example, at a thickness of 3 nm, the phase coherency is 0.03. The calculated result of the phase coherency of the sap/Co (x nm)/Pt(2 nm) structure is shown as Fig. 4(a) in the main text.

APPENDIX E: MICROMAGNETIC SIMULATION FOR AMPLITUDES OF SPIN WAVES

The amplitude of spin waves is related to the magnetic susceptibility given by

$$\chi(\omega, k) = \frac{\gamma \mu_0 H_{\text{dem}} \begin{bmatrix} \gamma \mu_0 H_z - i\alpha\omega & -i\omega \\ i\omega & \gamma \mu_0 H_y - i\alpha\omega \end{bmatrix}}{\omega_r^2 - \omega^2 - i2\omega\Delta\omega}, \quad (\text{E1})$$

where H_{dem} is the demagnetization field, $\omega_r (= \gamma \mu_0 \sqrt{H_y H_z})$ is the resonance frequency, ω is the excitation frequency, $\Delta\omega (= \gamma \mu_0 \alpha (H_y + H_z)/2)$ is the resonance linewidth due to damping α , and $\mu_0 H_y$ and $\mu_0 H_z$ are effective fields transverse to \mathbf{m} , respectively. In our system,

$$H_y = H_{\text{ext}} + Jk^2, \quad H_z = H_{\text{ext}} + H_{\text{dem}} + Jk^2, \quad (\text{E2})$$

where $J = 2A_{\text{ex}}/\mu_0 M_s$ and A_{ex} is the exchange stiffness constant. From the magnetic susceptibility, the magnon amplitude (m_z) can be derived as

$$m_z \propto \int_0^{\infty} d\omega h[\omega(k)] \text{Im}[\chi_{22}]. \quad (\text{E3})$$

Here, excitation strength $h[\omega(k)]$ and Fourier transform of laser pulse $f[\omega(k)]$ are given by

$$h[\omega(k)] = \frac{f[\omega(k)]}{d}, \quad (\text{E4})$$

$$f[\omega(k)] = \exp\left[-\frac{\sigma^2 \omega(k)^2}{2}\right], \quad (\text{E5})$$

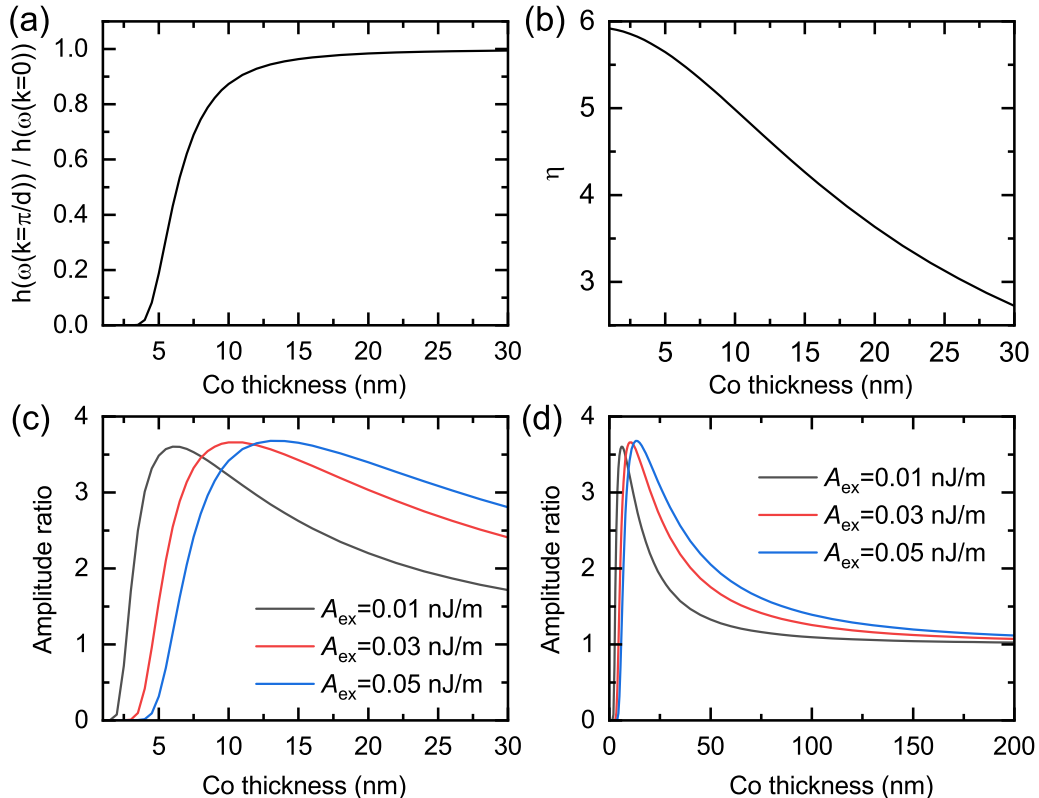


FIG. 8. Co thickness dependences of the excitation strength ratio, η , and the amplitude ratio r . (a) Excitation strength ratio. (b) Ratio constant η . (c), (d) Amplitude ratio for different exchange stiffness constants (A_{ex}). [(c) for Co thickness <30 nm, (d) for Co thickness <200 nm].

where σ is the laser pulse width, d is the Co film thickness. As a result, the amplitude ratio r of $k = \pi/d$ mode to $k = 0$ mode is given as,

$$r = \frac{m_z(k = \pi/d)}{m_z(k = 0)}. \quad (\text{E6})$$

In the small damping limit and using $H_{\text{dem}}, Jk^2 \gg H_{\text{ext}}$,

$$r \approx \frac{h(\omega(k = \pi/d))}{h(\omega(k = 0))} \sqrt{\frac{H_{\text{dem}} J \pi^2}{H_{\text{ext}} (H_{\text{dem}} d^2 + J \pi^2)}}. \quad (\text{E7})$$

Here, we define $\eta = \sqrt{\frac{H_{\text{dem}} J \pi^2}{H_{\text{ext}} (H_{\text{dem}} d^2 + J \pi^2)}}$ and $\frac{h(\omega(k=\pi/d))}{h(\omega(k=0))}$ is the excitation strength ratio. In Fig. 8, we plot Co thickness dependences of the excitation strength ratio, η , and the amplitude ratio r . For a thin film ($d < 3$ nm), the magnon frequency of $k = \pi/d$ mode is too high to be excited by the laser pulse. Thus, the excitation strength ratio is almost zero for very thin films [Fig. 8(a)]. On the other hand, η monotonically decreases with increasing the Co thickness [Fig. 8(b)] as expected from the definition of η . As a result, the amplitude ratio r first increases and then decreases with the Co thickness [Fig. 8(c) and Fig. 8(d)]. Importantly, r is larger than 1 except for very thin Co ranges because of the excitation strength ratio ≈ 1 and $\eta > 1$.

-
- [1] F. Bloch, *Z. Phys.* **61**, 206 (1930).
- [2] N. W. Ashcroft and N. D. Mermin, *Solid State Physics* (Brooks/Cole Cengage Learning, Belmont, 1976).
- [3] S. O. Demokritov, V. E. Demidov, O. Dzyapko, G. A. Melkov, A. A. Serga, B. Hillebrands, and A. N. Slavin, *Nature (London)* **443**, 430 (2006).
- [4] S. Kaka, M. R. Pufall, W. H. Rippard, T. J. Silva, S. E. Russek, and J. A. Katine, *Nature (London)* **437**, 389 (2005).
- [5] F. B. Mancoff, N. D. Rizzo, B. N. Engel, and S. Tehrani, *Nature (London)* **437**, 393 (2005).
- [6] Y. Kajiwara, K. Harii, S. Takahashi, J. Ohe, K. Uchida, M. Mizuguchi, H. Umezawa, H. Kawai, K. Ando, K. Takanashi, S. Maekawa, and E. Saitoh, *Nature (London)* **464**, 262 (2010).
- [7] R. Lebrun, A. Ross, S. A. Bender, A. Qaiumzadeh, L. Baldrati, J. Cramer, A. Brataas, R. A. Duine, and M. Kläui, *Nature (London)* **561**, 222 (2018).
- [8] R. Hertel, W. Wulfhekel, and J. Kirschner, *Phys. Rev. Lett.* **93**, 257202 (2004).
- [9] T. Schneider, A. A. Serga, B. Leven, B. Hillebrands, R. L. Stamps, and M. P. Kostylev, *Appl. Phys. Lett.* **92**, 022505 (2008).
- [10] V. E. Demidov, J. Jersch, K. Rott, P. Krzyszczyk, G. Reiss, and S. O. Demokritov, *Phys. Rev. Lett.* **102**, 177207 (2009).
- [11] A. Khitun, M. Bao, and K. L. Wang, *J. Phys. D: Appl. Phys.* **43**, 264005 (2010).
- [12] A. V. Chumak, A. A. Serga, and B. Hillebrands, *Nat. Commun.* **5**, 4700 (2014).
- [13] K. Vogt, F. Y. Fradin, J. E. Pearson, T. Sebastian, S. D. Bader, B. Hillebrands, A. Hoffmann, and H. Schultheiss, *Nat. Commun.* **5**, 3727 (2014).
- [14] V. V. Kruglyak, S. D. Demokritov, and D. Grundler, *J. Phys. D: Appl. Phys.* **43**, 264001 (2010).
- [15] B. Lenk, H. Ulrichs, F. Garbs, and M. Münzenberg, *Phys. Rep.* **507**, 107 (2011).
- [16] A. V. Chumak, V. I. Vasyuchka, A. A. Serga, and B. Hillebrands, *Nat. Phys.* **11**, 453 (2015).
- [17] M. Tsoi, A. G. M. Jansen, J. Bass, W.-C. Chiang, V. Tsoi, and P. Wyder, *Nature (London)* **406**, 46 (2000).
- [18] M. Madami, S. Bonetti, G. Consolo, S. Tacchi, G. Carlotti, G. Gubbiotti, F. B. Mancoff, M. A. Yar, and J. Åkerman, *Nat. Nanotech.* **6**, 635 (2011).
- [19] M. van Kampen, C. Jozsa, J. T. Kohlhepp, P. LeClair, L. Lagae, W. J. M. de Jonge, and B. Koopmans, *Phys. Rev. Lett.* **88**, 227201 (2002).
- [20] B. Lenk, G. Eilers, J. Hamrle, and M. Münzenberg, *Phys. Rev. B* **82**, 134443 (2010).
- [21] T. Satoh, Y. Terui, R. Moriya, B. A. Ivanov, K. Ando, E. Saitoh, T. Shimura, and K. Kuroda, *Nat. Photon.* **6**, 662 (2012).
- [22] I. Razdolski, A. Alekhin, N. Ilin, J. P. Meyburg, V. Roddatis, D. Diesing, U. Bovensiepen, and A. Melnikov, *Nat. Commun.* **8**, 150007 (2017).
- [23] M. L. M. Laliu, P. L. J. Helgers, and B. Koopmans, *Phys. Rev. B* **96**, 014417 (2017).
- [24] M. L. M. Laliu, R. Lavrijsen, R. A. Duine, and B. Koopmans, *Phys. Rev. B* **99**, 184439 (2019).
- [25] A. J. Schellekens, K. C. Kuiper, R. de Wit, and B. Koopmans, *Nat. Commun.* **5**, 4333 (2014).
- [26] G.-M. Choi, B.-C. Min, K.-J. Lee, and D. G. Cahill, *Nat. Commun.* **5**, 4334 (2014).
- [27] G.-M. Choi, J. H. Oh, D.-K. Lee, S.-W. Lee, K. W. Kim, M. Lim, B.-C. Min, K.-J. Lee, and H.-W. Lee, *Nat. Commun.* **11**, 1482 (2020).
- [28] S. Chikazumi, *Physics of Ferromagnetism* (Clarendon Press, Oxford, 1997).
- [29] H. A. Alperin, O. Steinsvoldi, G. Shirane, and R. Nathans, *J. Appl. Phys.* **37**, 1052 (1966).
- [30] G. Shirane, V. J. Minkiewicz, and R. Nathans, *J. Appl. Phys.* **39**, 383 (1968).
- [31] X. Liu, M. M. Steiner, R. Sooryakumar, G. A. Prinz, R. F. C. Farrow, and G. Harp, *Phys. Rev. B* **53**, 12166 (1996).
- [32] M. Grimsditch, E. E. Fullerton, and R. L. Stamps, *Phys. Rev. B* **56**, 2617 (1997).
- [33] A. Yoshihara, J.-I. Mawatari, H. Sato, S. Okamoto, O. Kitakami, and Y. Shimada, *Phys. Rev. B* **67**, 134435 (2003).
- [34] M. D. Stiles and A. Zangwill, *Phys. Rev. B* **66**, 014407 (2002).
- [35] Y. Tserkovnyak, A. Brataas, and G. E.W. Bauer, *Phys. Rev. Lett.* **88**, 117601 (2002).
- [36] Y. Tserkovnyak, A. Brataas, G. E.W. Bauer, and B. I. Halperin, *Rev. Mod. Phys.* **77**, 1375 (2005).
- [37] A. Kapelrud and A. Brataas, *Phys. Rev. Lett.* **111**, 097602 (2013).
- [38] Y. Tserkovnyak, E. M. Hankiewicz, and G. Vignale, *Phys. Rev. B* **79**, 094415 (2009).

- [39] R. Vollmer, M. Etzkorn, P. S. Anil Kumar, H. Ibach, and J. Kirschner, *Phys. Rev. Lett.* **91**, 147201 (2003).
- [40] G. Zahnd, L. Vila, V. T. Pham, M. Cosset-Cheneau, W. Lim, A. Brenac, P. Laczkowski, A. Marty, and J. P. Attané, *Phys. Rev. B* **98**, 174414 (2018).
- [41] K.-H. Ko and G.-M. Choi, *J. Magn. Magn. Mater.* **510**, 166945 (2020).
- [42] R. Carey, D. M. Newman, and B. W. Thomas, *Thin Solid Films* **51**, 251 (1978).
- [43] M. Suzuki, H. Muraoka, Y. Inaba, H. Miyagawa, N. Kawamura, T. Shimatsu, H. Maruyama, N. Ishimatsu, Y. Isohama, and Y. Sonobe, *Phys. Rev. B* **72**, 054430 (2005).
- [44] K. Imasaka, R. V. Pisarev, L. N. Bezmaternykh, T. Shimura, A. M. Kalashnikova, and T. Satoh, *Phys. Rev. B* **98**, 054303 (2018).